# Direct conversion of $CO_2$ to light aromatics by composite ZrCr-C/ZSM-5 catalyst

Ying Shi [a], Weizhe Gao [a,*], Kangzhou Wang [b,*], Lijun Zhang [a], Haozhe Feng [a], Xiaoyu Guo [a], Yingluo He [a], Xiaobo Feng [c], Qiang Liu [d], Tao Li [d], Yufeng Pan [d], Qingxiang Ma [e], Noritatsu Tsubaki [a,*]

[a] Department of Applied Chemistry, School of Engineering, University of Toyama, Gofuku 3190, Toyama 930-8555, Japan
[b] School of Materials and New Energy, Ningxia University, Yinchuan, Ningxia 750021, China
[c] Jiangsu Province Engineering Research Center of Fine Utilization of Carbon Resources, China University of Mining & Technology, Xuzhou, Jiangsu 221116, China
[d] National Engineering Research Center of Coal Gasification and Coal-Based Advanced Materials Shandong Energy Group Co., Ltd., Jinan 250014, China
[e] State Key Laboratory of High-efficiency Utilization of Coal and Green Chemical Engineering, College of Chemistry and Chemical Engineering, Ningxia University, Yinchuan, Ningxia 750021, China

## ARTICLE INFO

## ABSTRACT

In recent years, the direct and efficient conversion of $CO_2$ to light aromatics (BTX: benzene, toluene and xylene) has attracted wide attention. It not only reduces the $CO_2$ concentration in the atmosphere but also provides a promising non-petroleum technology to produce BTX. Herein, a composite ZrCr-C/ZSM-5 catalyst was developed for $CO_2$ to BTX. Different with conventional $SiO_2$ modification method, the HZSM-5 zeolite was modified by amorphous carbon (C) through a facile modified impregnation method. The amorphous C could enter the internal channel of HZSM-5 zeolite and poison partial acid sites. In $CO_2$ to BTX reaction, after introducing 1.45 wt % C on HZSM-5 zeolite, BTX selectivity increased from 36.2% to 45.4%. In addition, the ZrCr-1.45 C/ZSM-5 catalyst exhibited 46.9% BTX selectivity with 13.5% $CO_2$ conversion, under 5.0 MPa, 360 °C and 4800 mL/$g_{cat}$/h. This work not only paves a new strategy to modify HZSM-5 zeolite but also provides an efficient composite catalyst for direct conversion of $CO_2$ to BTX.

## 1. Introduction

Light aromatics (BTX: benzene, toluene and xylene) are irreplaceable raw materials in petrochemical industries for the production of plastics, polymers and so on [1–3]. The annual global demand for commodity aromatic monomers (especially BTX) surpasses 140 million metric tons, with a growing of 2–6% every year [4,5]. Traditionally, BTX are mainly obtained from the catalytic reforming of naphtha [6–8]. However, the decreasing petroleum resource cannot follow the growing demand of BTX in the future [9,10]. It is urgent to develop some non-petroleum technologies to synthesize BTX [11].

Recently, the efficient utilization of non-petroleum energy resources (such as coal, natural gas, biomass, organic waste and so on) has been attracted much attention [12]. Direct conversion of $CO_2$ to BTX is a hot topic. It not only partially relieves the $CO_2$ emission for solving environmental issues but also opens an avenue for synthesis BTX by non-petroleum route [13–17]. Generally, $CO_2$ hydrogenation to BTX

contains two routes: modified Fischer-Tropsch synthesis (FTS) route and methanol route [18–20]. In modified FTS route, $CO_2$ was firstly transformed to CO by reverse water-gas shift (RWGS) reaction and subsequently CO was converted to BTX by classical FTS reaction [21]. Although the modified FTS route exhibited higher $CO_2$ conversion, the obtained products were complex and widely distributed. For methanol route, $CO_2$ was firstly transformed to methanol and then methanol was converted to BTX by typical methanol-to-aromatics reaction [22]. In this catalytic system, zeolite catalyst played a vital role due to its excellent ability for hydrocarbon oligomerization and aromatization reactions [23,24]. Among these zeolite catalysts, HZSM-5 zeolite was the most promising candidate since its suitable pore size to produce benzene, toluene and para-Xylene (shape selectivity) [25]. During the methanol-to-aromatics reaction process, BTX firstly formed in the microporous of HZSM-5 zeolite and subsequently alkylated to heavy aromatics ($C_{9+}$ aromatics) on the external surface of HZSM-5 zeolite [26]. To further improve the selectivity of BTX, the key point was precise

controlling the acidity of HZSM-5 zeolite [27].

To date, many works have reported some methods to eliminate the external acid sites of zeolite and further improve BTX selectivity [28–30]. The most attractive method was to construct a core-shell structure catalyst with HZSM-5 as the core and non-acidic membrane as the shell. For non-acidic membrane, Silicalite-1 and amorphous $SiO_2$ have been investigated extensively [31,32]. Silicalite-1 as an Al-free zeolite, not only without acid sites but also has the same pore size with HZSM-5, and these properties were beneficial for the diffusion of BTX [33]. Traditionally, HZSM-5@Silicate-1 core-shell zeolite was prepared by the hydrothermal method [34]. However, this method not only produced a large amount of wastewater but also spent a lot of time. Compared with HZSM-5@Silicate-1 core-shell zeolite, HZSM-5@$SiO_2$ core-shell zeolite could be obtained by a simple and time-saving chemical liquid deposition method [35,36]. But the size of amorphous $SiO_2$ molecular was larger than the pore size of HZSM-5. The amorphous $SiO_2$ would block the channel of HZSM-5 zeolite and prevent the diffusion of BTX [37,38]. Hence, the development of other powerful methods for increasing BTX selectivity was necessary. On the other hand, as a complementary strategy, doped some metals (such as Zn or Ga) on HZSM-5 also could enhance the aromatics selectivity [39–41].

In this work, a novel C/ZSM-5 zeolite was firstly reported and applied in $CO_2$ to BTX reaction. Different with conventional hydrothermal and liquid deposition methods, the C/ZSM-5 zeolite was achieved through a facile modified impregnation method. This preparation method not only completely avoided the employment of large amounts of solvents but also more efficient. The amorphous C could cover partial inside and external acid sites of HZSM-5. For catalytic performances, after introducing 1.45 wt% C on original HZSM-5 zeolite, BTX selectivity increased from 36.2% to 45.4%. Moreover, the ZrCr-1.45 C/ZSM-5 composite catalyst exhibited 46.9% BTX selectivity with 13.5% $CO_2$ conversion, under 5.0 MPa, 360 °C and 4800 mL/$g_{cat}$/h. In addition, the C/ZSM-5 zeolite exhibited higher BTX selectivity than C/Zn/ZSM-5 and C/Ga/ZSM-5 (C doping on Zn/ZSM-5 or Ga/ZSM-5) zeolites. Furthermore, it was worth noting that the preparation method of C/ZSM-5 zeolite was simpler than HZSM-5@Silicate-1 and HZSM-5@$SiO_2$ core-shell zeolites. This work not only opens an avenue for modifying HZSM-5 zeolite but also contributes an effective solution for the direct conversion of $CO_2$ to valuable chemical feedstocks.

## 2. Experimental section

### 2.1. Catalyst preparation

ZrCr catalyst was prepared by a sol-gel combined with $CO_2$ supercritical drying method. Typically, 8.56 g $ZrO(NO_3)_2 \bullet 2\ H_2O$ and 1.61 g $Cr(NO_3)_3 \bullet 9\ H_2O$ were dissolved in 75 mL deionized water and 225 mL ethanol. The mixture solution was stirred at room temperature for 0.5 h. Subsequently, 1.95 g formamide and 30.2 g 1,2-propylene oxide were added into the above aqueous solution. After stirring 1 h at the same temperature, the precursor was moved to 70 °C water bath to gelation for 2 h. Then, the gel was washed by ethanol and transformed to an autoclave. $CO_2$ gas was fed into the autoclave by a high-pressure pump. After the pressure reached 7.5 MPa, the temperature was gradually increased to 260 °C and maintained for 1 h. Finally, ZrCr catalyst was obtained after calcining at 500 °C for 3 h.

ZSM-5 sample ($SiO_2/Al_2O_3 = 105$) was purchased from Mizusawa Industrial Chemicals Co. Before using, the ZSM-5 zeolite sample was firstly calcined at 550 °C for 6 h. Subsequently, 2 g ZSM-5 zeolite sample was dispersed and stirred in 100 mL $NH_4NO_3$ aqueous solution (1 M) at 80 °C for 5 h. This ion exchange process was repeated twice. After filtrating and washing by deionized water, the sample was dried at 100 °C overnight and calcined at 550 °C for 5 h. The obtained sample was marked as HZSM-5.

Zn/ZSM-5 and Ga/ZSM-5 zeolites were prepared by ion exchange method. 2 g HZSM-5 was added in 200 mL $Zn(NO_3)_2 \bullet 6\ H_2O/Ga$

$(NO_3)_3 \bullet 8\ H_2O$ aqueous solution (0.1 M). After stirring at 80 °C for 12 h, the sample was washed by deionized water for three times and collected by filtration. The product was dried overnight at 100 °C and calcined 550 °C for 5 h. The obtained samples were marked as Zn/ZSM-5 and Ga/ZSM-5.

The C/ZSM-5 zeolite was prepared by a modified impregnation method. Briefly, carboxymethyl cellulose and 1.5 g HZSM-5 zeolite were ground together. Subsequently, deionized water was dropwise added into the mixture under ultrasound-assisted for 1 h. Finally, the product was dried at 100 °C overnight and calcined at 650 °C for 3 h under a flow of $N_2$ (40 mL/min). The sample was marked as $x$C/ZSM-5 ($x$ represented the weight percent of C). The weight percent of C was controlled by adjusting the weight of carboxymethyl cellulose.

The composite catalyst was prepared by physical mixing. Oxide and zeolite catalysts with the weight ratio of 1/1 were mixed in an agate mortar for 3 min, and then pressed, crushed, and sieved to 20–40 meshes.

### 2.2. Catalyst characterization

XRD spectrum of the catalyst was collected using a Rigaku RINT 2400 system diffractometer by employing Cu-Kα (40 KV, 40 mA) radiation at room temperature.

$H_2$ temperature programmed reduction ($H_2$-TPR) profile was recorded by a BELCAT-B-TT catalyst analyzer equipped with thermal conductive detector (TCD). Firstly, 50 mg catalyst was pretreated at 150 °C for 1 h under a flow of pure He to remove the physically adsorbed water, and then followed by temperature programmed reduction in $H_2$ from 40 to 700 °C with a heating rate of 10 °C/min.

$CO_2$ temperature programmed desorption ($CO_2$-TPD) profile was measured by a BELCAT-B-TT catalyst analyzer equipped with a TCD. In the procedure for pretreated, 50 mg sample was treated at 400 °C for 2 h under a flow of pure $H_2$. Then the sample was cooled down to 50 °C and saturated with $CO_2$. Subsequently, the sample was purged by He at the same temperature to remove the physically adsorbed $CO_2$. Finally, the procedure was performed from 50 to 800 °C with a heating rate of 10 °C/min under a flow of He.

$NH_3$ temperature programmed desorption ($NH_3$-TPD) profile was performed by a BELCAT-B-TT catalyst analyzer equipped with a TCD. In the procedure for pretreated, 50 mg sample was treated at 500 °C for 1 h under a flow of pure He (30 mL/min). Then the sample was cooled down to 50 °C and saturated with $NH_3$. Subsequently, the sample was purged by He at the same temperature to remove the physically adsorbed $NH_3$. Finally, the procedure was performed from 50 to 800 °C with a heating rate of 10 °C/min under a flow of He.

Scanning electron microscopy (SEM) images were observed by JEOL JSM-6360LV with JED-2300 energy dispersive spectroscopy (EDS) attachment.

X-ray photoelectron spectroscopy (XPS) spectra were carried out by a Thermo Fisher Scientific ESCALAB 250Xi multifunctional spectroscopy equipped by an in-situ reduction pretreatment chamber.

The elemental analysis was carried out to quantitatively obtain the carbon content on a vario M-CUBE analyzer. Elemental composition of ZrCr sample was determined by a Philips Magix-601 wave-dispersive X-ray fluorescence (XRF) spectrometry.

Thermogravimetry (TG) measurement was carried out over 50 mg sample in air with flow rate of 30 mL/min using TA-60WS thermal analyzer (Shimadzu). The program was performed at the heating rate of 10 °C/min from room temperature to 900 °C.

The surface area, pore volume and size of different zeolites were measured by $N_2$ physical adsorption using a Micromeritics 3Flex 2MP instrument. Before sample analysis, the catalysts were degassed at 300 °C for 5 h.

Pyridine (Py) and 2,6-di-tert-butylpyridine (DTBPy) adsorbed FTIR spectra were performed with a Bruker Tensor 27 FTIR spectrometer. Firstly, the zeolite sample was pressed into a thin wafer. After degassing

at 350 °C and $1 \times 10^{-2}$ Pa for 2 h, the wafer was exposed in the Py/DTBPy vapor for probing molecule adsorption (room temperature, 30 min). Then the FTIR spectrum was recorded after evacuation at 150 °C for 30 min.

## 2.3. Catalytic activity test

The catalytic performance was performed in a high pressure fixed-bed reactor with the internal diameter of 6 mm. Prior to the reaction, all catalysts were reduced by pure $H_2$ (60 mL/min) at 400 °C for 2 h. After cooling down to room temperature, the feed gas (24.06 vol% $CO_2$, 3.01 vol% CO, 3.01 vol% Ar and $H_2$ balance) was fed in the reactor. In feed gas, the introduction of trace CO could inhibit the process of the reverse water-gas shift reaction, therefore depressing the undesired CO selectivity [13]. The reaction temperature and pressure were 360 °C and 5 MPa, respectively. The reaction effluents were quantitatively analyzed online with three gas chromatographs (GC-8A, Shimadzu), one equipped with TCD and active charcoal column for Ar, CO, $CH_4$, and $CO_2$ analysis; one equipped with flame ionization detector (FID) and HP-PLOT/Q column for hydrocarbons analysis; while another equipped with FID and HP-INNOWAX column to further identify the xylene isomers. Between the reactor and gas chromatograph, the temperature of steel tube was 200 °C to inhibit the condensation of products. Using Ar as an inner standard, $CO_2$ conversion and hydrocarbons C-mol selectivity were calculated according to the following equations:

$$CO_2 Conversion = \frac{CO_{2inlet} - CO_{2outlet}}{CO_{2inlet}} \times 100\%$$

Where $CO_{2inlet}$ and $CO_{2outlet}$ represented mole fractions of $CO_2$ at the inlet and outlet, respectively.

$$Sel_{C_nH_m} = \frac{nC_nH_{m\ outlet}}{\sum_1^n nC_nH_{m\ outlet}} \times 100\%$$

CO was formed via the RWGS reaction, and its selectivity was calculated according to:

$$CO\ \ selectivity = \frac{CO_{outlet} - CO_{inlet}}{CO_{2inlet} - CO_{2outlet}} \times 100\%$$

Where $CO_{inlet}$ and $CO_{outlet}$ represented mole fractions of CO at the inlet and outlet, respectively.

CO was not included in hydrocarbon and MeOH/DME selectivity calculation due to its different selectivity calculation method.

The yield of BTX was calculated according to:

$$Yield\ \ of\ \ \ BTX = CO_2 Conversion \times (1 - CO\ \ sel.) \times BTX\ \ selectivity$$

## 3. Results and discussion

### 3.1. Characterization of ZrCr catalyst

The XRD pattern of ZrCr oxide was shown in Fig. S1 (Supporting Information). The ZrCr oxide exhibited the characteristic peaks, which were assigned to the $ZrO_2$ phase (JCPDS: NO. 3–640). Specifically, no characteristic diffraction peaks of Cr oxide were detected, indicating the good dispersion of Cr on $ZrO_2$ phase. XRF analysis demonstrated the elemental composition of ZrCr oxide, the molar ratio of Zr/Cr was displayed in Table S1. The $N_2$ adsorption/desorption isotherm and pore-size distribution curve of ZrCr oxide were displayed in Fig. S2. Furthermore, the ZrCr oxide exhibited 141.9 $m^2/g$ surface area (Table S1). It was obviously higher than traditional co-precipitation method [29]. This result indicated that the sol-gel combined with $CO_2$ supercritical drying method was beneficial to enhance surface area of oxide catalyst. The SEM images of ZrCr oxide were displayed in Fig. S3. As seen, the ZrCr oxide exhibited a blocky morphology and a smooth external surface. The EDS mapping further shown the elemental

distributions of Zr and Cr. Moreover, no aggregation of Cr was found. This result implied that the Cr evenly distributed on the surface of $ZrO_2$ oxide, and this was consistent with the XRD result.

To investigate the reduction behavior of ZrCr oxide, $H_2$-TPR technology was employed. As shown in Fig. S4, $H_2$-TPR profile exhibited a signal reduction peak, which was attributed to the reduction of $Cr_2O_3$ to CrO [42]. In addition, it was difficult to reduce $ZrO_2$ before 700 °C. The basic property of ZrCr oxide was determined by $CO_2$-TPD, as shown in Fig. S5. The ZrCr oxide displayed three $CO_2$ desorption peaks at 112 °C, 366 °C and 574 °C, which were derived from weak, medium and strong basic sites, respectively.

### 3.2. Characterization of zeolite catalysts

The XRD patterns of different zeolites were shown in Fig. 1(a). All zeolites exhibited the typical characteristic peaks, which were associated with MFI structure. For C/ZSM-5 zeolites, no peaks belonging to amorphous C were observed, indicating the good dispersion of C on HZSM-5 zeolite. In detail, the weight percent of C was detected by elemental analysis method and the results were shown in Table 1. Furthermore, TG technology was employed to measure the C loss of different C/ZSM-5 zeolites, the results were shown in Fig. S6 and Table 1. As displayed in Table 1, with increasing the weight of carboxymethyl cellulose, the C loading increased from 0.44 to 2.81 wt%. At the same time, the C loading was similar with C loss. For C/ZSM-5 zeolites, the C loading weight percent of all samples were controlled to lower than 3 wt%. The reasons were that: amorphous C could enter the micropores of zeolite due to the fact that the size of amorphous C was smaller than the pore size of HZSM-5 zeolite, excessive C on the internal acid sites of zeolite would affect the catalytic performance of zeolite. The $N_2$ adsorption/desorption isotherms, surface areas and pore volumes of different zeolites were displayed in Fig. 1(b) and Table 1. The significant $N_2$ adsorption could be observed at low relative pressure, indicating the presence of micropores structure and the introduction of C did not block the micropores of HZSM-5 zeolite. With increasing the C content, surface area decreased from 371.3 to 333.9 $m^2/g$; the micropore surface area decreased from 294.7 to 265.6 $m^2/g$. These results suggested that the amorphous C enter the inside of HZSM-5 zeolite. In addition, the pore-size distribution curves of different C/ZSM-5 zeolites were displayed in Fig. S7. It was obvious that all zeolites exhibited same pore-size distribution. The surface morphologies of different zeolites were observed by SEM technology, the images as shown in Fig. 2. The original HZSM-5 zeolite exhibited an approximately elliptical shape. After modifying by amorphous C, no significant differences were observed. The additional amorphous C did not change the shape of HZSM-5 zeolite. Moreover, these zeolites displayed similar particle size.

The overall acidic properties of all zeolites were investigated by $NH_3$-TPD, Py-FTIR and DTBPy-FTIR technologies. Fig. 3(a) exhibited the $NH_3$-TPD profiles of different zeolites. The original HZSM-5 zeolite displayed two obvious $NH_3$ desorption peaks: the peak at around 148 °C was attributed to weak acid sites, whereas the peak at around 385 °C was ascribed to the medium strong acid sites. It was obvious that, with increasing the C content, the two peaks shifted to lower temperature and the area of medium strong acid sites decreased. These results suggested that the introduction of C decreased the acidity of zeolite and reduced the amounts of medium strong acid sites. The Py-FTIR spectra were carried out to detect the acid site types of zeolites, the results were shown in Fig. 3(b). The peaks around 1452 and 1541 $cm^{-1}$ were attributed to Lewis and Brønsted acid sites, respectively. With increasing the C content on HZSM-5 zeolite, the amounts of Lewis and Brønsted acid sites decreased. This result indicated that the introduction of C simultaneously reduced Lewis and Brønsted acid sites. In addition, DTBPy-FTIR profiles were employed to determine the external surface acid sites of zeolite, as shown in Fig. 3(c). The band was ascribed to the external surface acid sites. As seen, with increasing C content, the signal of external acid sites decreased. However, some external acid sites were
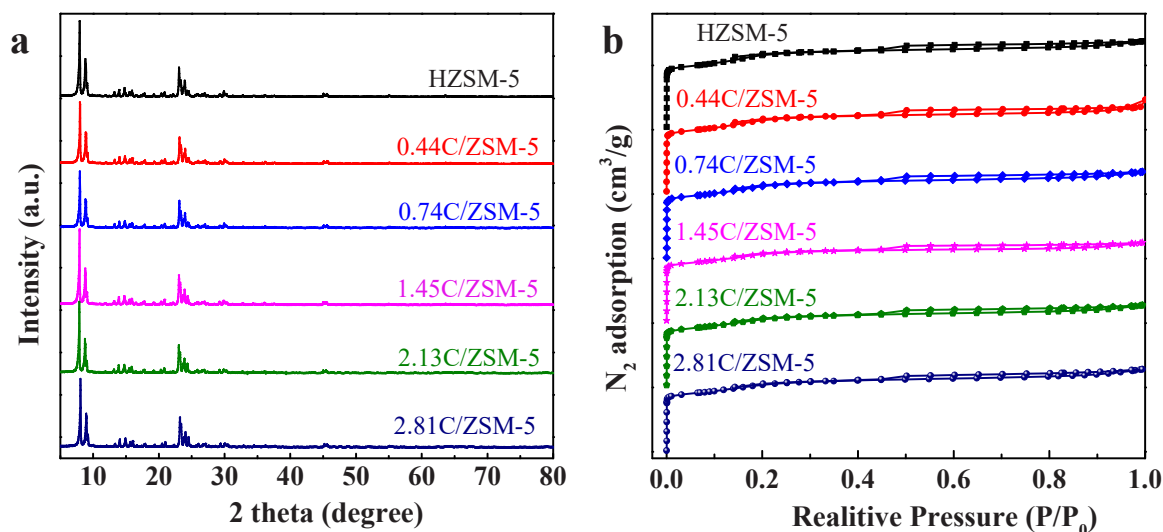
**Fig. 1.** (a) XRD patterns and (b) $N_2$ adsorption/desorption isotherms of different zeolites.

**Table 1**
C content and structure of different zeolites.

| Sample | C loading (wt%)[a] | C loss (wt %)[b] | $S_{BET}$ (m²/g)[c] | $S_{micro}$ (m²/g)[d] | $V_{total}$ (cm³/g)[e] | $V_{micro}$ (cm³/g)[f] | $V_{meso}$ (cm³/g)[g] |
|---|---|---|---|---|---|---|---|
| HZSM-5 | - | - | 371.3 | 294.7 | 0.212 | 0.121 | 0.091 |
| 0.44 C/ZSM-5 | 0.44 | 0.57 | 367.9 | 293.2 | 0.210 | 0.122 | 0.088 |
| 0.74 C/ZSM-5 | 0.74 | 0.88 | 360.5 | 287.5 | 0.208 | 0.120 | 0.088 |
| 1.45 C/ZSM-5 | 1.45 | 1.68 | 340.4 | 274.5 | 0.192 | 0.118 | 0.074 |
| 2.13 C/ZSM-5 | 2.13 | 2.51 | 338.8 | 269.8 | 0.197 | 0.114 | 0.083 |
| 2.81 C/ZSM-5 | 2.81 | 3.32 | 333.9 | 265.6 | 0.197 | 0.112 | 0.085 |

[a] C weight percent was detected by elemental analysis;
[b] C loss was obtained by TG technology;
[c] the total surface area was calculated using the BET method;
[d] the micropore surface area was determined by the t-Plot method;
[e] the total pore volume was estimated with the nitrogen adsorption at $p/p_0 = 0.99$;
[f] the micropore volume was determined by the t-Plot method;
[g] the mesopore volume was obtained as $V_{total} - V_{micro}$.

still detected, indicating the amorphous C enter the inside pores of HZM-5 zeolite. In order to investigate the external surface information of C/ZSM-5, XPS technology was further employed. The Al 2p XPS spectra of different zeolites were displayed in Fig. 3(d). All zeolites exhibited a peak at around 75.0 eV, which was belonged to the presence of Al on the external surface of zeolites. We thought the amorphous C could not as shell encapsule HZSM-5 zeolite by this modified impregnation method, the reasons were that: the content of introduced amorphous C was small; the amorphous C entered the inside pores of HZSM-5 zeolite.

### 3.3. Effects of different C/ZSM-5 zeolites on $CO_2$ hydrogenation performance

The effects of different C/ZSM-5 zeolites on $CO_2$ hydrogenation performance were compared and the results were displayed in Fig. 4,

Table S2 and Table S3. Firstly, ZrCr-HZSM-5 composite catalyst was tested under the reaction conditions of 360 °C, 5 MPa and GHSV = 2400 mL/$g_{cat}$/h. This catalyst exhibited 16.6% $CO_2$ conversion, 66.2% aromatics selectivity, 36.2% BTX selectivity (in hydrocarbons) and 64.5% CO selectivity. After impregnating 0.44 wt% C on the HZSM-5 zeolite, $CO_2$ conversion slightly decreased to 16.3% and aromatics increased to 72.2%, respectively. The reason was that the introduction of amorphous C reduced the acidity and amounts of medium strong acid sites of HZSM-5 zeolite and inhibited the hydrogenation reaction of light olefins. Further increasing the weight percent of C from 0.44 to 2.81 wt %, $CO_2$ conversion did not change significantly. The aromatics selectivity firstly increased from 72.2% to 75.8% and then decreased to 72.2%. The $C_{2-4}$ olefins selectivity gradually increased from 3.0% to 6.6%. Moreover, $C_{2-4}$ paraffins selectivity displayed the opposite trend with the aromatics selectivity. In addition, the BTX selectivity firstly increased from 43.4% to 45.4% and then decreased to 41.0%. The reason was attributed to the fact that amorphous C entering the micropore of HZSM-5 zeolite and suppressing partial acid sites. When the weight percent of C was 1.45 wt%, the highest aromatics and BTX selectivities were obtained. In addition, compared original HZSM-5 with 1.45 C/ZSM-5 zeolites, $CO_2$ conversion remained stable, BTX selectivity increased from 36.2% to 45.4%, respectively. Moreover, the undesirable $CH_4$ was controlled within 2%. This result indicated that appropriate amorphous C could cover partial acid sites of HZSM-5 zeolite and effectively enhance BTX selectivity. The BTX yield from different C/ZSM-5 zeolites as exhibited in Table S2. As seen, ZrCr-HZSM-5 catalyst exhibited 2.1% BTX yield. With increasing the weight percent of C from 0 to 2.13 wt%, the yield of BTX firstly increased and then decreased. Although 1.45 C/ZSM-5 exhibited higher BTX selectivity than 0.74 C/ZSM-5 zeolite, the BTX yield was slightly lower than 0.74 C/ZSM-5 zeolite. The reason was that the 0.74 C/ZSM-5 zeolite displayed higher $CO_2$ conversion and lower CO selectivity. With increasing the weight percent of C to 2.81 wt%, 2.7% BTX yield was obtained, due to the relatively high $CO_2$ conversion.

On the other hand, the original HZSM-5 zeolite exhibited 6.7% para-Xylene (PX) selectivity (Table S3). After impregnating C on the HZSM-5 zeolite, PX selectivity first slightly increased to 8.8% and then decreased to 7.9%. When the weight percent of C was 1.45 wt%, the highest PX selectivity was obtained. Compared with typically HZSM-5@SiO$_2$ core-shell zeolite, C/ZSM-5 zeolite could not significantly enhance PX selectivity. This phenomenon was attributed to the different external surface acid sites. The size of amorphous $SiO_2$ was larger than amorphous C. The deposition of $SiO_2$ on the external surface of HZSM-5 zeolite could effectively passivate the external acid sites. But the pores
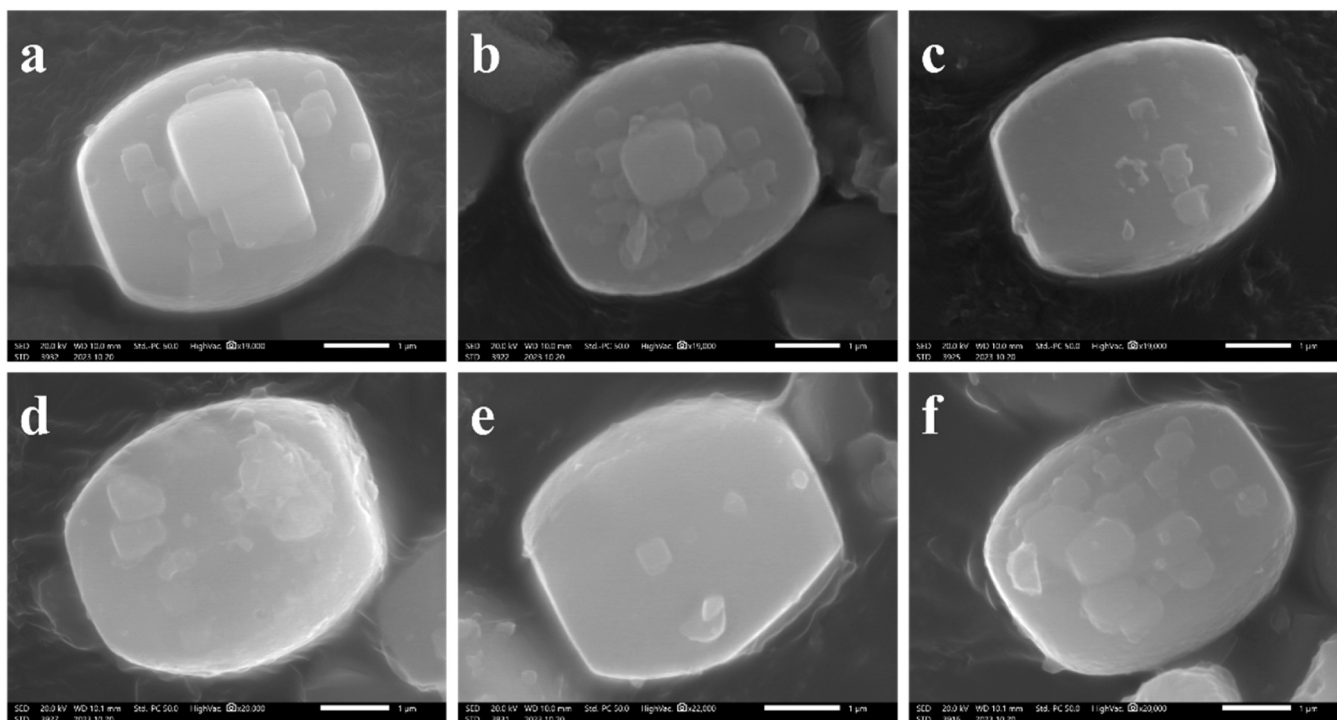
**Fig. 2.** SEM images of (a) HZSM-5, (b) 0.44 C/ZSM-5, (c) 0.74 C/ZSM-5, (d) 1.45 C/ZSM-5, (e) 2.13 C/ZSM-5 and (f) 2.81 C/ZSM-5 zeolites.
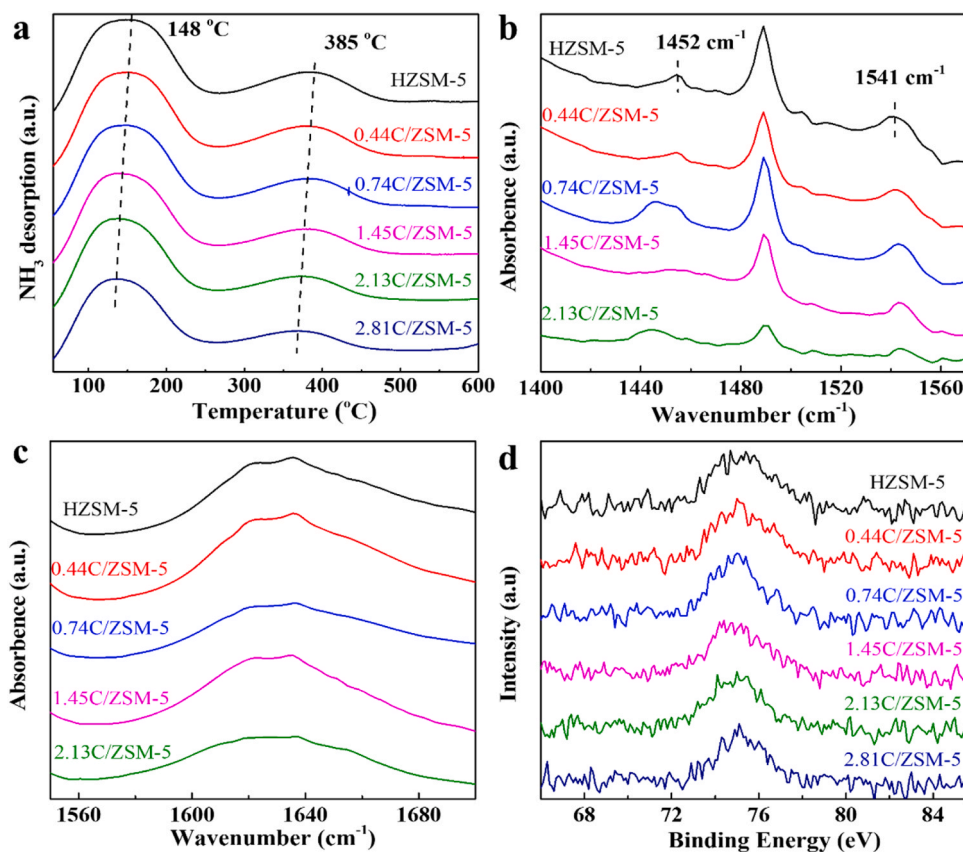


**Fig. 3.** (a) NH$_3$-TPD, (b) Py-FTIR, (c) DTBPy-FTIR and (d) Al 2p XPS spectra of different zeolites.

of zeolite would be blocked partially. In addition, on the external surface of HZSM-5 zeolite, the confined space between SiO$_2$ was not conducive to the isomerization and alkylation of PX. Hence, the PX selectivity

increased significantly. However, the preparation of HZSM-5@SiO$_2$ core-shell zeolite required using a large amount of SiO$_2$, the weight percent of SiO$_2$ exceeded 30% [26]. The trace amount of SiO$_2$ could not
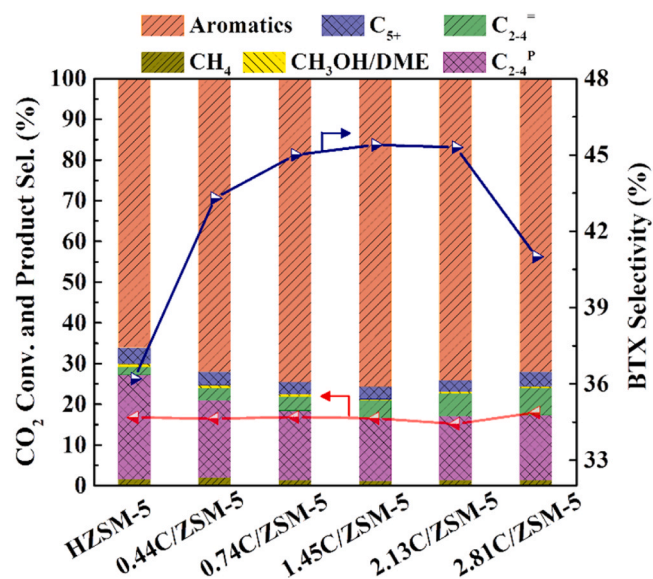
**Fig. 4.** Catalytic performances of ZrCr oxide with different zeolites. CO₂ hydrogenation reaction conditions: 360 °C, 5.0 MPa, (24.06 vol% CO₂, 3.01 vol% CO, 3.01 vol% Ar and H₂ balance), GHSV = 2400 mL/g_cat/h and time on stream (TOS) = 8 h, oxide/zeolite mass ratio = 1:1, powder-mixing.
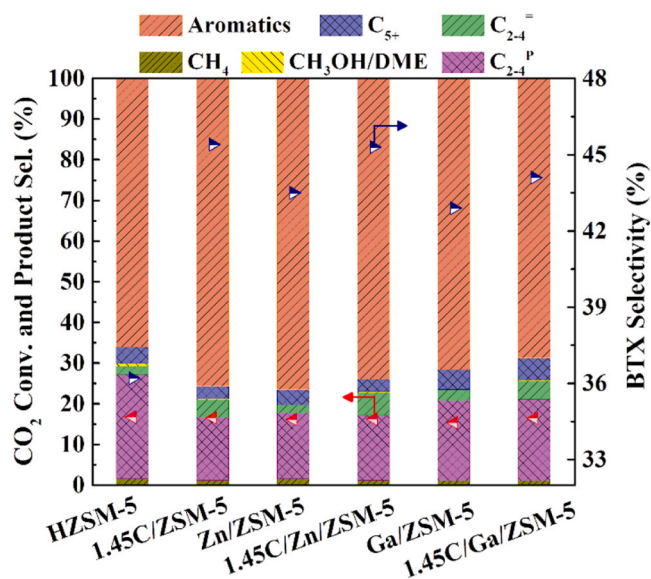


**Fig. 5.** Catalytic performances of ZrCr oxide with different zeolites. CO₂ hydrogenation reaction conditions: 360 °C, 5.0 MPa, (24.06 vol% CO₂, 3.01 vol% CO, 3.01 vol% Ar and H₂ balance), GHSV = 2400 mL/g_cat/h and time on stream (TOS) = 8 h, oxide/zeolite mass ratio = 1:1, powder-mixing.

dramatically enhance PX selectivity. As for C/ZSM-5 zeolite, the trace amount of amorphous C also could not completely cover the external acid sites of HZSM-5 zeolite. In detail, PX would be isomerized to other xylenes or alkylated to heavy aromatics due to the presence of external acidity and insufficient space constraints. In turn, with increasing the weight percent of C, excess carbon would enter the micropores of the HZSM-5 zeolite and cover partial internal acid sites, decreasing PX selectivity. But the C/ZSM-5 shown an obvious advantage: it could significantly enhance BTX selectivity while keeping aromatics selectivity stable.

### 3.4. Effects of different zeolites on CO₂ hydrogenation performance

In recent years, the metal modified zeolites have attracted wide attention, such as Zn/ZSM-5, Ga/ZSM-5 and so on. In this work, Zn and Ga were doped on the original HZSM-5 zeolite by the typical ion-exchange method, and these samples were marked as M/ZSM-5 (M = Zn or Ga). The catalytic performances were displayed in Fig. 5, Table S4 and Table S5. In detail, the ZrCr-Zn/ZSM-5 catalyst exhibited 16.0% CO₂ conversion, 68.7% CO selectivity, 76.7% aromatics and 43.5% BTX selectivities. For ZrCr-Ga/ZSM-5 catalyst, 15.2% CO₂ conversion, 65.8% CO selectivity, 71.8% aromatics and 42.9% BTX selectivities were obtained. Compared with ZrCr-HZSM-5 catalyst, the ZrCr-Zn/ZSM-5 and ZrCr-Ga/ZSM-5 catalysts exhibited relatively high aromatics and BTX selectivities. These results were attributed to the dehydrogenation capability of Zn²⁺ and Ga³⁺, which was helpful in improving the performance of methanol to aromatics reaction. After adding 1.45 wt% amorphous C on M/ZSM-5 zeolites, aromatics selectivity decreased, BTX and PX selectivities increased slightly. We speculate the reason may be that the amorphous C poisoned the active sites of Zn/Ga. As a result, the ZrCr-1.45 C/ZSM-5 catalyst shown higher BTX selectivity than ZrCr-1.45 C/M/ZSM-5 catalyst. In Table S4, 1.45 C/ZSM-5 zeolite displayed higher BTX yield than 1.45 C/Zn/ZSM-5 and 1.45 C/Ga/ZSM-5 zeolites. This was due to 1.45 C/ZSM-5 zeolite exhibited higher CO₂ conversion, BTX selectivity and lower CO selectivity.

### 3.5. Effects of integration manners on CO₂ hydrogenation performance

In composite catalytic system, the integration manner of oxide and
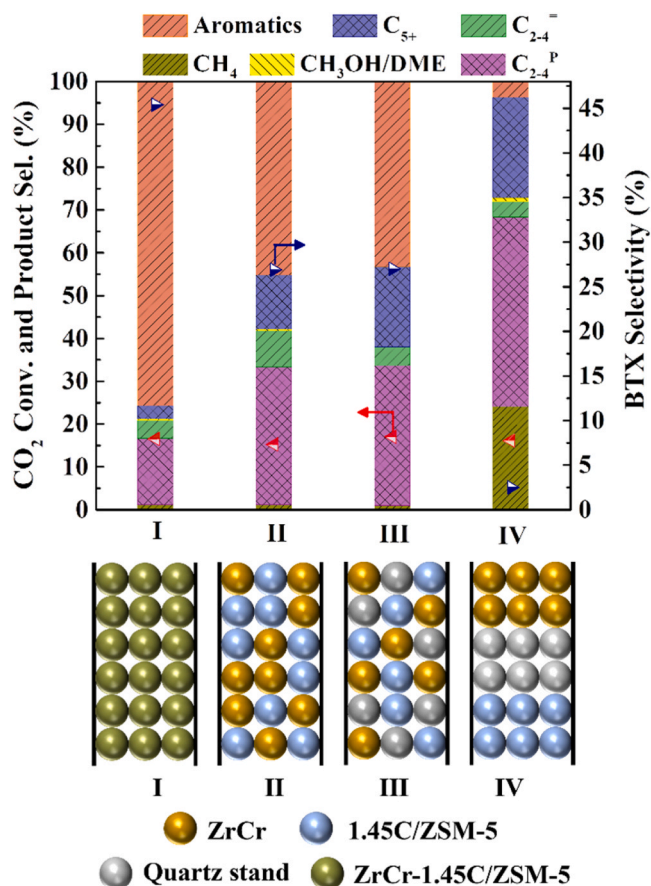


**Fig. 6.** Catalytic performances of ZrCr-1.45 C/ZSM-5 catalyst with different integration manners. I, II, III and IV represent powder-mixing, granule-mixing, granule-mixing with quartz sand, and dual bed, respectively. CO₂ hydrogenation reaction conditions: 360 °C, 5.0 MPa, (24.06 vol% CO₂, 3.01 vol% CO, 3.01 vol% Ar and H₂ balance), GHSV = 2400 mL/g_cat/h and time on stream (TOS) = 8 h, oxide/zeolite mass ratio = 1:1.

zeolite catalysts plays a key role. The effects of different integration manners on $CO_2$ hydrogenation performance were compared, as shown in Fig. 6, Table S6 and Table S7. When the integration manner was typical powder-mixing, the ZrCr-1.45 C/ZSM-5 catalyst exhibited 16.4% $CO_2$ conversion, 65.9% CO selectivity, 75.8% aromatics selectivity and 45.4% BTX selectivity. Adjusting the integration manner to granule-mixing, aromatics and BTX selectivities decreased from 75.8% to 45.3% and 45.4% to 26.9%, respectively. After mixing catalyst particles with quartz stand, 16.9% $CO_2$ conversion, 70.5% CO selectivity, 43.3% aromatics and 27.0% BTX selectivities were realized. Further increasing the distance between ZrCr and 1.45 C/ZSM-5 catalyst, dual bed (ZrCr and 1.45 C/ZSM-5 catalysts were separated by quartz stand in one reactor) was employed. Over this spatial system, 16.0% $CO_2$ conversion, 68.2% CO selectivity, 3.7% aromatics and 2.5% BTX selectivities were obtained. With increasing the distance between oxide and zeolite catalysts, $CO_2$ conversion and CO selectivity did not change significantly; $CH_4$ selectivity dramatically increased from 1.0% to 24.0%; $C_{2-4}$ paraffins selectivity sharply increased from 15.5% to 44.3%. In addition, $C_{2-4}$ olefins and $CH_3OH$/DME selectivity not changed significantly. But the aromatics and BTX selectivities decreased from 75.8% to 3.7% and 45.4% to 2.5%, respectively. These results indicated that the intimately spatial contact of ZrCr oxide and 1.45 C/ZSM-5 zeolite was beneficial for increasing aromatics and BTX selectivities. The longer distance would affect the diffusion of intermediate. In this catalytic system, methanol as an intermediate could desorb from ZrCr oxide and subsequently diffuse into the micropores of 1.45 C/ZSM-5 zeolite. When the two components were close to each other, the diffusion of generated intermediates become faster. Increasing the distance between ZrCr oxide and 1.45 C/ZSM-5 zeolite, the produced methanol from ZrCr was difficult to reach the 1.45 C/ZSM-5 zeolite to initiate the subsequent methanol to aromatics reaction. On the other hand, the formation of methanol and methane were parallel competitive reactions [43]. The close distance was beneficial for removing and consuming of methanol, which shifted the thermodynamic equilibrium to methanol synthesis instead of the generation of methane (Table S6). In addition, after mixing oxide and zeolite by powder-mixing method, some external acid sites of 1.45 C/ZSM-5 zeolite were covered by oxide, some side reactions were inhibited. In turn, the longer distance leaded to the complete exposed acid sites of zeolites, and subsequently the light olefins were converted to paraffins by the over-hydrogenation reaction. In addition, with increasing the distance between ZrCr oxide and 1.45 C/ZSM-5 zeolite, the BTX yield sharply decreased from 2.5% to 0.1% (Table S6). The main reason was the dramatic decrease for BTX selectivity. For direct conversion of $CO_2$ to BTX, the powder-mixing integration manner could effectively inhibit other side reactions of olefins and improve BTX selectivity. Moreover, under the powder-mixing condition, the influence of methanol partial pressure on product selectivity was investigated, the results were shown in Fig. 8, Table S8 and Table S9. As seen, after introducing additional methanol, $CO_2$ conversion and CO selectivity decreased significantly. This was attributed to the introduction of methanol inhibited the $CO_2$ conversion. With gradual increasing the methanol partial pressure, aromatics selectivity sharply decreased from 75.8% to 8.8%. Under high methanol partial pressure, only 6.7% BTX selectivity and 0.2% BTX yield were obtained. Furthermore, light olefins were converted into light paraffins and $C_{5+}$. This result suggested that, for powder-mixing integration manner, low methanol partial pressure was beneficial for the formation of aromatics.

### 3.6. Effects of GHSV on $CO_2$ hydrogenation performance

The effects of GHSV on $CO_2$ hydrogenation performance were investigated, as shown in Fig. 7, Table S10 and Table S11. With increasing the GHSV from 2400 to 19200 mL/$g_{cat}$/h, $CO_2$ conversion decreased from 16.4% to 6.5%, CO selectivity increased from 65.9% to 86.6%. In addition, $C_{2-4}$ paraffins selectivity decreased from 15.5% to 4.5% and $C_{2-4}$ olefins selectivity increased from 4.3% to 29.1%.
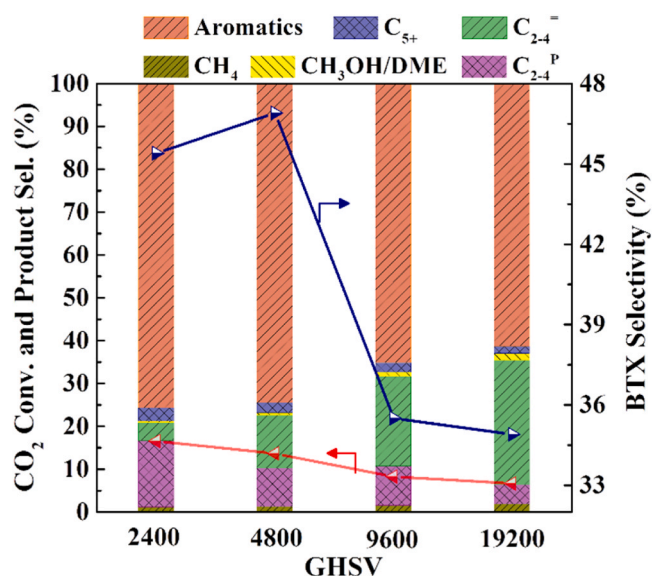


**Fig. 7.** Catalytic performances of ZrCr-1.45 C/ZSM-5 catalyst with different GHSV (mL/$g_{cat}$/h). $CO_2$ hydrogenation reaction conditions: 360 °C, 5.0 MPa, (24.06 vol% $CO_2$, 3.01 vol% CO, 3.01 vol% Ar and $H_2$ balance), time on stream (TOS) = 8 h, oxide/zeolite mass ratio = 1:1, powder-mixing.

Aromatics selectivity decreased from 75.8% to 61.4%. However, BTX selectivity exhibited a volcanic pattern, which firstly increased and then decreased. When the GHSV was 4800 mL/$g_{cat}$/h, BTX selectivity reached highest 46.9%. Although lower GHSV was beneficial for the formation of BTX and the conversion of $C_{2-4}$ olefins due to the long contact time, appropriate enhancing GHSV could increase BTX selectivity. The reason was that appropriate increasing GHSV would shorten the contaction of BTX with external acid sites and inhibit the reaction of BTX to heavy aromatics. Meanwhile, with increasing GHSV, BTX yield sharply decreased from 2.5% to 0.3% due to the $CO_2$ conversion decreasing and CO selectivity increasing (Table S10). On the other hand, with GHSV increasing, the light olefins selectivity increased significantly. This result suggested that the light olefines might be acted as the intermediates in aromatization reaction. The suggested reaction pathway for methanol to aromatics on ZSM-5 zeolite was exhibited in Fig. S9 [44,45]. In addition, the stability of ZrCr-1.45 C/ZSM-5 was evaluated at 360 °C, 5.0 MPa and 4800 mL/$g_{cat}$/h. The result was displayed in Fig. S10. During 60 h, $CO_2$ conversion, $CH_4$, $C_{2-4}$ paraffins and $C_5^+$ selectivities remained stable. With $C_{2-4}$ olefins selectivity increasing, aromatics selectivity decreased. Moreover, the BTX selectivity almost kept stable after 45 h.

### 4. Conclusions

In summary, we developed a unique C/ZSM-5 zeolite by a modified impregnation method and applied it in $CO_2$ hydrogenation to BTX reaction. The C/ZSM-5 zeolites with different C loadings were characterized in detail. Compared with original HZSM-5 zeolite, after introducing amorphous C, BTX selectivity increased significantly. When the weight percent of C was 1.45 wt%, higher BTX selectivity was obtained. Under the reaction conditions of 360 °C, 5.0 MPa and 4800 mL/$g_{cat}$/h, the composite ZrCr-1.45 C/ZSM-5 catalyst exhibited 46.9% BTX selectivity. The amorphous C could enter the internal channel of HZSM-5 zeolite and poison partial acid sites. Compared with traditional methods for modifying HZSM-5 zeolite, this modified impregnation method was simpler. Furthermore, it was worth noting that the C/ZSM-5 zeolite could significantly enhance BTX selectivity while keeping aromatics selectivity stable. Moreover, in this catalytic system, the effects of different zeolites, integration manners and GHSV for $CO_2$ hydrogenation performance were systematically investigated. This work developed a

promising strategy for modified HZSM-5 zeolite and provided a new zeolite for synthesis BTX by $CO_2$ hydrogenation.

## CRediT authorship contribution statement

**Noritatsu Tsubaki:** Writing – review & editing, Conceptualization, Data curation, Methodology, Project administration, Resources, Supervision. **Weizhe Gao:** Writing – review & editing, Resources, Methodology. **Yufeng Pan:** Formal analysis, Software. **Qingxiang Ma:** Methodology. **Ying Shi:** Writing – original draft, Methodology, Data curation. **Qiang Liu:** Formal analysis, Software. **Tao Li:** Formal analysis, Software. **Yingluo He:** Formal analysis. **Xiaobo Feng:** Formal analysis, Software. **Haozhe Feng:** Validation, Data curation. **Xiaoyu Guo:** Formal analysis, Data curation. **Kangzhou Wang:** Writing – review & editing, Resources, Methodology. **Lijun Zhang:** Validation, Data curation.

## Declaration of Competing Interest

The authors declare that they have no known competing financial interests or personal relationships that could have appeared to influence the work reported in this paper.

## Data availability

Data will be made available on request.

## Acknowledgments

## Appendix A. Supporting information

Supplementary data associated with this article can be found in the online version at doi:10.1016/j.apcatb.2024.124068.

## References

[1] D. Miao, Y. Ding, T. Yu, J. Li, X. Pan, X. Bao, ACS Catal. 10 (2020) 7389–7397.
[2] Z. Li, Y. Qu, J. Wang, H. Liu, M. Li, S. Miao, C. Li, Joule 3 (2019) 570–583.
[3] Y. Fu, Y. Ni, Z. Chen, W. Zhu, Z. Liu, J. Energy Chem. 66 (2022) 597–602.
[4] S. Kasipandi, J.W. Bae, Adv. Mater. 31 (2019) 1803390–1803407.
[5] A.E. Settle, L. Berstis, N.A. Rorrer, Y. Roman-Leshkóv, G.T. Beckham, R. M. Richards, D.R. Vardon, Green Chem. 19 (2017) 3468–3492.
[6] S. Wang, Z. Huang, Y. Luo, J. Wang, Y. Fang, W. Hua, Y. Yue, H. Xu, W. Shen, Catal. Sci. Technol. 10 (2020) 6562–6572.
[7] C. Zhou, J. Shi, W. Zhou, K. Cheng, Q. Zhang, J. Kang, Y. Wang, ACS Catal. 10 (2020) 302–310.
[8] P. Zhang, L. Tan, G. Yang, N. Tsubaki, Chem. Sci. 8 (2017) 7941–7946.
[9] W. Gao, L. Guo, Q. Wu, C. Wang, X. Guo, Y. He, P. Zhang, G. Yang, G. Liu, J. Wu, N. Tsubaki, Appl. Catal. B: Environ. 303 (2022) 120906.
[10] Y. Shi, Q. Zhou, Z. Qin, Z. Wu, W. Jiao, M. Dong, W. Fan, J. Wang, Microporous Mesoporous Mater. 324 (2021) 111308.
[11] C. Liu, J. Su, S. Liu, H. Zhou, X. Yuan, Y. Ye, Y. Wang, W. Jiao, L. Zhang, Y. Lu, Y. Wang, H. He, Z. Xie, ACS Catal. 10 (2020) 15227–15237.
[12] X. Yang, X. Su, D. Chen, T. Zhang, Y. Huang, Chin. J. Catal. 41 (2020) 561–573.
[13] W. Gao, L. Guo, Y. Cui, G. Yang, Y. He, C. Zeng, A. Taguchi, T. Abe, Q. Ma, Y. Yoneyama, N. Tsubaki, ChemSusChem 13 (2020) 6541–6545.
[14] Y. Jiang, K. Wang, Y. Wang, Z. Liu, X. Gao, J. Zhang, Q. Ma, S. Fan, T.-S. Zhao, M. Yao, J. CO2 Util. 67 (2023) 102321.
[15] Z. Liu, X. Gao, K. Wang, T. Atchimarungsri, J. Tian, P. Reubroycharoen, Q. Ma, T.-S. Zhao, N. Tsubaki, J. Zhang, Fuel Process. Technol. 241 (2023) 107628.
[16] B. Zhao, Y. Zhao, P. Liu, Y. Men, X. Meng, Y. Pan, J. Chinese, Struct. Chem. 41 (2022) 2204012–2204021.
[17] C.P. Wan, R. Cao, Y.B. Huang, Chin. J. Struct. Chem. 41 (2022) 2205001–2205014.
[18] J. Wei, Q. Ge, R. Yao, Z. Wen, C. Fang, L. Guo, H. Xu, J. Sun, Nat. Commun. 8 (2017) 15174.
[19] A. Ramirez, A. Dutta Chowdhury, A. Dokania, P. Cnudde, M. Caglayan, I. Yarulina, E. Abou-Hamad, L. Gevers, S. Ould-Chikh, K. De Wispelaere, V. van Speybroeck, J. Gascon, ACS Catal. 9 (2019) 6320–6334.
[20] W. Wang, R. He, Y. Wang, M. Li, J. Liu, J. Liang, S. Yasuda, Q. Liu, M. Wu, N. Tsubaki, Chem. Eur. J. 29 (2023) e202301135.
[21] X. Cui, P. Gao, S. Li, C. Yang, Z. Liu, H. Wang, L. Zhong, Y. Sun, ACS Catal. 9 (2019) 3866–3876.
[22] W. Zhou, K. Cheng, J. Kang, C. Zhou, V. Subramanian, Q. Zhang, Y. Wang, Chem. Soc. Rev. 48 (2019) 3193–3228.
[23] J. Wei, R. Yao, Q. Ge, Z. Wen, X. Ji, C. Fang, J. Zhang, H. Xu, J. Sun, ACS Catal. 8 (2018) 9958–9967.
[24] Q. Zhang, J. Yu, A. Corma, Adv. Mater. 32 (2020) 2002927.
[25] C. Wang, L. Zhang, X. Huang, Y. Zhu, G. Li, Q. Gu, J. Chen, L. Ma, X. Li, Q. He, J. Xu, Q. Sun, C. Song, M. Peng, J. Sun, D. Ma, Nat. Commun. 10 (2019) 4348.
[26] Y. Wang, W. Gao, S. Kazumi, H. Li, G. Yang, N. Tsubaki, Chem. Eur. J. 25 (2019) 5149–5153.
[27] T. Wang, C. Yang, P. Gao, S. Zhou, S. Li, H. Wang, Y. Sun, Appl. Catal. B-Environ. 286 (2021) 119929.
[28] J. Zhang, W. Qian, C. Kong, F. Wei, ACS Catal. 5 (2015) 2982–2988.
[29] L. Zhang, W. Gao, F. Wang, C. Wang, J. Liang, X. Guo, Y. He, G. Yang, N. Tsubaki, Appl. Catal. B: Environ. 328 (2023) 122535.
[30] K. Miyake, Y. Hirota, K. Ono, Y. Uchida, S. Tanaka, N. Nishiyama, J. Catal. 342 (2016) 63–66.
[31] T. Wang, Y. Xu, C. Shi, F. Jiang, B. Liu, X. Liu, Catal. Sci. Technol. 9 (2019) 3933–3946.
[32] F. Yang, Y. Fang, x liu, X. Liu, D. Muir, A. Maclennan, X. Zhu, Ind. Eng. Chem. Res. 58 (2019) 13879–13888.
[33] A. Ghorbanpour, A. Gumidyala, L.C. Grabow, S.P. Crossley, J.D. Rimer, ACS Nano 9 (2015) 4006–4016.
[34] Y. Wang, L. Tan, M. Tan, P. Zhang, Y. Fang, Y. Yoneyama, G. Yang, N. Tsubaki, ACS Catal. 9 (2019) 895–901.
[35] W. Zhou, S. Shi, Y. Wang, L. Zhang, Y. Wang, G. Zhang, X. Min, K. Cheng, Q. Zhang, J. Kang, Y. Wang, ChemCatChem 11 (2019) 1681–1688.
[36] X. Han, J. Zuo, D. Wen, Y. Yuan, Chin. J. Catal. 43 (2022) 1156–1164.
[37] H. Wang, P. Gao, S. Li, T. Wang, C. Yang, J. Li, T. Lin, L. Zhong, Y. Sun, Chem. Catal. 2 (2022) 779–796.
[38] D. Miao, X. Pan, F. Jiao, Y. Ji, G. Hou, L. Xu, X. Bao, Catal. Sci. Technol. 11 (2021) 4521–4528.
[39] J. Zhang, L. Wang, Z. Wu, H. Wang, C. Wang, S. Han, F. Xiao, Ind. Eng. Chem. Res. 58 (2019) 15453–15458.
[40] J. Zhang, X. Zhu, S. Zhang, M. Cheng, M. Yu, G. Wang, C. Li, Catal. Sci. Technol. 9 (2019) 316–326.
[41] X. Su, G. Wang, X. Bai, W. Wu, L. Xiao, Y. Fang, J. Zhang, Chem. Eng. J. 293 (2016) 365–375.
[42] P. Xia, S. Zuo, F. Liu, C. Qi, Catal. Commun. 41 (2013) 91–95.
[43] W. Zhou, S. Shi, Y. Wang, L. Zhang, Y. Wang, G. Zhang, X. Min, K. Cheng, Q. Zhang, J. Kang, Y. Wang, ChemCatChem 11 (2019) 1681–1688.
[44] D. Wang, Z. Xie, M.D. Porosoff, J.G. Chen, Chem 7 (2021) 2277–2311.
[45] A. Ramirez, A.D. Chowdhury, A. Dokania, P. Cnudde, M. Caglayan, I. Yarulina, E. Abou-Hamad, L. Gevers, S. Ould-Chikh, K.D. Wispelaere, V.V. Speybroeck, J. Gascon, ACS Catal. 9 (2019) 6320–6334.